C. R. Mecanique 338 (2010) 461–473

Contents lists available at ScienceDirect

Comptes Rendus Mecanique

www.sciencedirect.com

Inverse problems

An inverse hyper-spherical harmonics-based formulation for reconstructing 3D volumetric lung deformations

Une formulation inverse reposant sur les harmoniques hypersphériques pour la reconstruction 3D du mouvement du poumon

Anand P. Santhanam [a,e], Yugang Min [b], Sudhir P. Mudur [c], Abhinav Rastogi [a], Bari H. Ruddy [d], Amish Shah [e], Eduardo Divo [f], Alain Kassab [f,*], Jannick P. Rolland [g], Patrick Kupelian [h]

[a] *College of Optics and Photonics, University of Central Florida, Orlando, FL 32816 2450, USA*
[b] *College of Electrical Engineering and Computer Science, University of Central Florida, Orlando, FL 32816 2450, USA*
[c] *Concordia University, Canada*
[d] *Department of Health and Public Affairs, University of Central Florida, Orlando, FL 32816 2450, USA*
[e] *Department of Radiation Oncology, M.D. Anderson Cancer Center, Orlando, USA*
[f] *Mechanical, Material and Aerospace Engineering, University of Central Florida, Orlando, FL 32816 2450, USA*
[g] *Institute of Optics, University of Rochester, USA*
[h] *Department of Radiation Oncology, University of California, Los Angeles, USA*

ARTICLE INFO

Article history:
Available online 19 August 2010

Keywords:
Biomechanics
Inverse problems
3D lung dynamics
Hyper-spherical harmonics

Mots-clés :
Biomécanique
Problèmes inverses
Dynamique 3D du poumon
Harmoniques hypersphériques

ABSTRACT

A method to estimate the deformation operator for the 3D volumetric lung dynamics of human subjects is described in this paper. For known values of air flow and volumetric displacement, the deformation operator and subsequently the elastic properties of the lung are estimated in terms of a Green's function. A Hyper-Spherical Harmonic (HSH) transformation is employed to compute the deformation operator. The hyper-spherical coordinate transformation method discussed in this paper facilitates accounting for the heterogeneity of the deformation operator using a finite number of frequency coefficients. Spirometry measurements are used to provide values for the airflow inside the lung. Using a 3D optical flow-based method, the 3D volumetric displacement of the left and right lungs, which represents the local anatomy and deformation of a human subject, was estimated from 4D-CT dataset. Results from an implementation of the method show the estimation of the deformation operator for the left and right lungs of a human subject with non-small cell lung cancer. Validation of the proposed method shows that we can estimate the Young's modulus of each voxel within a 2% error level.

RÉSUMÉ

Une méthode d'estimation de l'opérateur associé à la description 3D des mouvements volumiques du poumon humain est présentée dans cet article. Pour des écoulements entrants d'air et des déplacements volumiques connus, l'opérateur et, ensuite, les propriétés élastiques du poumon sont estimés en termes d'une fonction de Green. L'opérateur est calculé à l'aide d'une transformation en harmoniques hypersphériques, qui facilite la prise en compte de l'hétérogénéité de l'opérateur au moyen d'un nombre fini de coefficients fréquentiels. Les écoulements entrants d'air sont estimés au moyen de données

* Corresponding author.
E-mail address: kassab@mail.ucf.edu (A. Kassab).

1631-0721/$ – see front matter
doi:10.1016/j.crme.2010.07.006

spirométriques. Au moyen d'une méthode optique 3D de mesure d'écoulements, les mouvements volumiques des poumons gauche et droit, représentant l'anatomie et les mouvements locaux d'un sujet humain, ont été estimès à l'aide de données 4D-CT. Les résultats issus de la mise en œuvre de la méthode comprennent l'estimation de l'opérateur de déformation pour les poumons gauche et droit d'un sujet humain atteint de cancer du poumon. La validation de la méthode montre que le module de Young peut être estimé dans chaque voxel à 2 % près.

1. Introduction

Understanding the physics and physiology of human organs enables clinicians to prescribe improved cancer treatment methodologies for patients. Advances in image-based and in-vitro experimental methods have enabled improved techniques for investigating the organ functionality. Of particular importance is the emergence of 3D and 4D medical imaging techniques that lead to effective medical visualization applications by coupling medical simulations with patient-specific 3D and 4D anatomical models capable of physically and physiologically realistic organ deformation [1]. The importance of modeling such organ movements can be seen in the case of lung radiation oncology that aims to expose the lung tumor of a human patient to radiation that ablates the tumor [2,3]. The efficacy of the radiation oncology procedure can be significantly improved when the movement of the lung tumor and the lung itself can be predicted in real-time during the radiation therapy. A physics and physiology-based 3D lung deformation system could further improve the image-guided radiotherapy procedures by estimating the lung surface and the tumor motion under different breathing conditions of the patient.

A key requirement to obtaining the subject-specific lung deformation for different breathing conditions is to estimate the elastic properties that control the deformation [1]. The importance of such estimation of subject-specific elastic properties is two-fold. First, from a deformation perspective, the estimated elastic properties can be used to deform lungs according to different breathing conditions. Second, from a pulmonary radiotherapy perspective, these estimated elastic properties provide an estimation of the expandability of the tissues surrounding the lung tumor that receive a significant amount of radiation as the lung tumor moves during breathing. Experts have extracted the lung tissue elasticity in terms of the Young's Modulus (YM) and the Poisson ratio using pressure–volume curves [4] for the elasticity representing the whole organ and in-vitro-based methods [5] for the elasticity of a sample lung tissue. Specifically the in-vitro-based methods are effective in finding the Poisson ratio by performing the axial and transverse strain measurement [6]. Table 1 shows the different values estimated for lung tissue elasticity reported in the literature using both image-based and in-vitro elastography. These tabulations show the range of values taken by the lung tissue across different subjects with different patho-physiological conditions. Simulation of the lung deformation while applying YM results from these methods is currently limited in the following ways. It is not feasible for the pressure–volume curve based methods to measure the heterogeneity of the lung tissue's elasticity in the case of diseased lungs. Taking into account the heterogeneity of the lung tissue's elasticity is important for modeling the motion of the lung tumor and its surrounding tissues which have significantly differing elastity values. Moreover, the in-vitro methods examine the lung tissue using a generic contact load force instead of the laminar fluid force that causes the alveoli to expand during breathing, which may lead to inaccurate measurements. There is clearly a need to develop methods for estimating subject-specific lung-tissue local elasticity.

The estimation of local elastic properties of the subject-specific lungs, which can then be used to simulate the breathing of 3D lung models according to different physical conditions, forms the focus of this paper. Specifically this paper discusses a method for estimating the volumetric lung physics- and physiology-based deformation operator for human subjects with Non-Small Cell Lung Cancer (NSCLC). This estimation is based on 4D-CT datasets that constitute a sequence of 3D-CT datasets representing volumetric lung anatomy at different air volumes and a pressure–volume curve, which closely represents the patient breathing. Our method, which enables a non-invasive estimation of subject-specific volumetric lung's elastic properties that control the lung deformation, is a key contribution of the paper. The deformation operator (also known as the deformation kernel or the transfer function of 3D lungs) associated with the lung is estimated as well. The estimated deformation operator takes into account the physics of the elastic interaction and the physiological effect implied by the rib cage and the diaphragm motion.

The article is structured as follows: Section 2 discusses related work in estimating tissue parameters using image-based methods; Section 3 discusses the proposed method of inverse deformation analysis; Section 4 presents the results of the inverse estimation analysis using 4D-CT datasets; Section 5 presents the validation results; Section 6 concludes the paper and discusses planned future work.

2. Related work

Recent advancements in imaging modalities such as ultrasound and magnetic resonance imaging (MRI) have led to an image-based estimation of tissue elasticity, which is referred to as elastography [16]. Such methods have been extensively applied to analysis of tumors and lesions in soft tissues. The common elastic parameter estimated is the YM, which is the ratio between the stress and strain at any particular link or estimated boundary [17]. Ultrasound-based elastography is

Table 1
YM values estimated for lungs by peers.

Elasticity	Source	Method
4 kPa (rat)	Fung, 1993 [7]	In-vitro measurements
4.5–6 kPa (rat)	Adler et al., 1998 [8]	CT excised lung
10 kPa (fibrotic lungs)	Ebihara et al., 2000 [9]	In-vitro elastography
1.53 ± 0.18 kPa (normal human)	Goss et al., 2003 [10]	MRI elastography
5–6 kPa (Guinea Pig)	Levental et al., 2007 [11]	In-vitro elastography
7.8 kPA (normal)	Brock et al., 2005 [12]	CT-, FE-based fitting
0.25–1 kPa (human)	Werner et al., 2008 [13]	CT-, FE-based fitting
0.1 kPa (normal humans) to 3 kPa (fibrotic lungs)	Liu et al., 2009 [14]	In-vitro elastography
5–30 kPa (ovine)	Cavalcante et al., 2005 [15]	In-vitro elastography

not currently used for extracting 3D lung's elastic parameters because of the lung's high air content. MRI has indeed been applied for studying the lung movements [18]. Variants of MRI such as spin-echo, gradient echo, and phase-contrast have been used to study the pulmonary vasculature. Currently, MRI-based elastography is only in initial stages of development [10,19]. These imaging methods currently face issues related to real-time imaging, which is important for analyzing 3D lung dynamics under intra-operative conditions. Additionally, from a mechanics perspective, these imaging methods do not consider both the 3D stress and the 3D strain components of deformation. They simply provide 3D strain.

Inverse Deformation (ID) methods allow the estimation of elastic tissue parameters of a 3D object given its known 3D deformation and applied force [16]. A significant amount of work has been done in exploring these methods for applications ranging from simple animations [20] to complex engineering simulations [21]. The general approach for the ID methods is to associate a mathematical representation such as Green's functions, Finite Difference Method (FDM), Finite Element Method (FEM), or thin plate deformation [22] to the 3D model's shape change [23,24].

Of particular importance as it relates to the work presented here is the Green's function, which has been used for modeling 3D lung deformations [25]. The deformation operator associated with the Green's function was estimated by first coupling a physically based deformation method to a 4D-CT dataset of a patient in a supine posture and then solving for the deformation operator. In this method a 3D polygonal lung model was extracted from a 3D-CT dataset at exhalation and then used to simulate the deformations. A single-compartment approach was used for representing the 3D lung polygonal model, meaning a 3D lung was considered as a single unit instead of a set of lobes. The deformation method used a kernel (Green's Function (GF) [23]) with surface-level boundary integrals. The method was further extended to show the feasibility of modeling the lung tumor motion based on the motion of the lung surface [25].

Spectral domain-based estimation methods have been previously investigated for a wide range of inverse problems from graphics to geophysics [26]. Of particular importance is the inverse rendering problems usage of Spherical Harmonics (SH) in the estimation of the Bi-Directional Reflectance Diffusion Function (BRDF), which has influenced the decision to use Hyper-Spherical Harmonics (HSH) in our problem [27]. Specifically, such a usage of harmonic functions stresses the fact that the computational complexity can be greatly simplified when estimating the functions in the frequency domain. Additionally, SH has been extensively used in the domain of geophysics in estimating geo-physical parameters such as the vibration [28]. SH-based formulation for deforming 3D lung surface dynamics in real-time has also been discussed in Santhanam et al. (2007) [29].

Hyper-Spherical Harmonics (HSH), which are the 3D extensions of SH, have also been well investigated in the nuclear physics domain to represent the angular momentum of electron rotations [30]. HSH formulations are based on the Gegenbauer polynomials, which are d-dimensional homogeneous polynomials. HSH expansions have been applied for a wide range of physics-based applications. A seminal work detailing the different applications of HSH for various domains related to the physics has been documented by Avery [30]. The application of HSH for reactive scattering has been pioneered by Kupperman et al. [31] and Aquilanti et al. [32]. Peterkop [33] presents a discussion on many-dimensional hydrogen-like wave functions using HSH. In the domain of quantum chemistry, Shibuya and Wulfman [34] discuss the many-center coulomb problem using HSH formulation. A Fourier expansion in d-dimensions using the HSH formulation has been investigated and discussed by Rudin [35].

There exist two limitations in the usage of SH and HSH. First is their low sensitivity to non-periodic high frequency data region, which is often eliminated as noise when the data is converted to the frequency domain [28]. In the case of volumetric lung deformations, such high frequency data are observed in the motion of lung tumor and its surrounding regions. The usage of a higher number of HSH coefficients leads to a significant increase in the computational and memory complexity with a low increase in the accuracy. The second limitation is their inability to account for local heterogeneity of the estimated values, which in the case of volumetric lung deformations may be observed by the deformation operator associated with each voxel point. As we shall see, it is these two limitations that are addressed by the proposed method.

3. Proposed method

In this section, we present our proposed method to estimate the 3D volumetric lung's deformation operator for modeling the volumetric lung deformations. The method is inspired by the usage of spherical harmonic transformations for inverse

rendering problems in the computer graphics domain [27]. From a computational perspective, an HSH-based spectral-domain method is employed for estimating the 3D volumetric lung tissue elasticity. A frequency domain formulation of the volumetric lung deformation operator is formulated using the HSH coefficients and which in turn are estimated from known values of applied force and displacement. In our formulation a mixed representation of HSH and the Wigner-d rotation transformations associated with the Special Orthogonal group 3 (SO(3)) is employed and forms one of the key contribution of the paper. Specifically, our proposed formulation uses HSH transformations for smooth data and Wigner-d rotation transformations for coarse data, which in our case is the airflow distribution inside the lungs and the volumetric lung displacement, respectively. Such a combination helps reduce the amount of data transformation error with a finite number of HSH and Wigner-d coefficients.

The modeling assumptions employed in the method discussed in this paper are previously discussed in detail in [25, 29,36] and [37]. They are as follows: a single-compartmental representation, in which the lung is considered as a single organ as opposed to multiple sub-organs, is considered. The non-uniform changes in the lung dimension and volume during breathing are caused by the (i) non-uniform changes in the thoracic cavity dimension because of the contraction of the diaphragm and the rotation of the rib-cage, (ii) the heterogeneous lung elasticity, and (iii) the regional variation in the airflow [37]. As previously discussed in [37], the lung tissue deformation is modeled to be an elastostatic interfaction of the airforce that flows inside the lung and the lung tissue. The blood flow and content in the lung tissue are assumed to be a constant during a single breathing. The lung airflow inside the lungs is considered to be determined by the gravity of the lung orientation.

The method is implemented in a two-step process. In the first step, a lung surface deformation operator is estimated from a given 4D-CT lung dataset using the method previously discussed in [36]. Specifically, at the end of the first step, the structural and functional constants associated with the surface points, which dictate the weighted Euclidean distance among the surface points, are estimated. In the second step, a volumetric lung deformation operator is estimated using the given 4D-CT lung dataset and the lung surface's structural and functional constants obtained in step 1. Specially, this volumetric deformation operator is estimated using the lung surface's structural and functional constants. A brief overview of the major steps involved in this estimation process is the following: the values estimated from the surface deformation operator are first projected onto the lung voxels. Using these values, an HSH parameterization, in which one of the angular coordinates is based on an intensity-based weighted distance computed using the projected structural and functional constants, is derived for the applied force as well as the displacement. Such a parameterization facilitates accounting for the heterogeneity of the deformation operator. The deformation operator is then estimated for each voxel using the proposed formulation. Once estimated, the deformation operator can be used to estimate the YM associated with each voxel of the 3D lung model.

Details of the parameterization used to estimate the HSH coordinates of each voxel in the lung are provided in Section 3.1, while the method used to incorporate the heterogeneous properties for the volumetric lung into the HSH parameterization is provided in Section 3.2. Wigner transformations and their HSH coefficients are then expanded in Section 3.3, and, finally, the method for estimation of the YM associated with each voxel using the HSH parameter estimation is given in Section 3.4.

3.1. Volumetric lung model parameterization

A given 3D lung model with the volumetric points or voxel positions given in the Cartesian coordinates in the form (X, Y, Z) is taken as input. As a first step, each voxel is assigned a hyper-spherical coordinate, which is of the form $(1, \theta, \varphi, \chi)$. The hyper-spherical coordinates in the above equation represent the azimuthal angle (θ), the elevation angle (φ), and the hyper-radial angle (χ) for (X, Y, Z). The volumetric points are parameterized using ray projection in such a way that the centroid of the lung voxels has the zero vector as the hyper-spherical coordinate values. The method for ray projection is previously discussed in [29]. Fig. 1 represents the ray projection from a lung voxel at the center of the lung to the surface boundary voxels. While the ray projection is computed for each voxel inside the lung to every other voxel, for clarity purposes, the image shows the rays only from the central voxel to the surface voxels. The r_c and r_c^{max} values are computed from the magnitude of such rays originating from each voxel. Let (X_c, Y_c, Z_c) be the center of the volumetric lung. Let r_c be the distance between any volumetric voxel (X, Y, Z) and (X_c, Y_c, Z_c). Let r_c^{max} be the distance between the farthest lung voxel and the center. We now set the value of χ as

$$\chi = \left(\frac{r_c}{r_c^{max}}\right) 2\pi \tag{1}$$

Let (X^n, Y^n, Z^n) be the normal of (X, Y, Z) from the center and r^n represent the normal distance, which is 1. Now the rest of the spherical coordinates are computed using the formulation:

$$\begin{aligned} X &= r^n \sin\theta \sin\varphi \\ Y &= r^n \sin\theta \cos\varphi \\ Z &= r^n \cos\varphi \end{aligned} \tag{2}$$

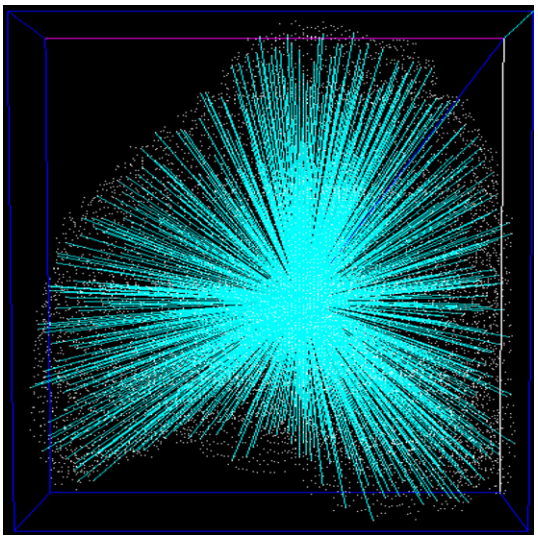

Fig. 1. Ray projection from the voxel at the center of the lung to the surface boundary voxels.

Table 2
Mathematical notation and description.

Notation	Description
(X, Y, Z)	The 3D location of a voxel point.
$(1, \theta, \varphi, \chi)$	The 3D hyper-spherical coordinate of a voxel point.
(X_C, Y_C, Z_C)	The 3D location of a center of a set of voxels.
R	The weighted distance from the center to any voxel.
r_c	The weighted distance from the center to the farthest voxel.
(X_n, Y_n, Z_n)	The normal of the voxel (X, Y, Z) from the center.
(X_b, Y_b, Z_b)	The voxel on the lung surface boundary.
(A, B, C)	The structural and functional constants estimated from the surface lung deformations.
Q_b^i	The weighted distance calculated for projecting the structural and functional constants estimated at the lung surface boundary to all the voxel points inside the lung.
Δq	The inter voxel distance.
(α, β, η)	The 3D hyper-spherical coordinate of a voxel with (X_c, Y_c, Z_c) as the center.
$(\theta_0, \varphi_0, \chi_0)$	The hyper-spherical coordinate of the origin.
ρ	The deformation operator.
D	The 3D displacement.
R	The SO(3) rotation group matrix.
F	The applied force.
S	The expansion of the SO(3) rotation group matrix in 3D.
D	The Hyper-Spherical Harmonic (HSH) coefficients of the displacement.
J	The Jacobi polynomial.
C	The Gegenbauer polynomial.
P	The Legendre polynomials.
N	The normalization factor associated with the HSH transformations.
Y	The HSH transform.
δ	The Dirac delta function.
ϑ	The Poisson ratio.
μ	The Lame's constant.
E	The Young's Modulus.

For given values of the (X, Y, Z), the azimuthal and elevation angles are computed by projecting a ray from the center (X_c, Y_c, Z_c) to (X, Y, Z) and measuring the angle made by the ray onto the two perpendicular planes that span the 3D domain.

3.2. Intensity-based volumetric projection

An important step towards the heterogeneous representation of the deformation operator is to account for the spatial variability of the tissue elastic properties. In order to do so, we introduce the following two modifications. First, the deformation operator for the lung tissue is estimated for each voxel separately by considering it as the center of the model. Thus the formulation is defined by considering each voxel as the origin and then the HSH coordinate transformation is performed for all the other voxels. Table 2 provides the mathematical notations used by the proposed method. Second, the

heterogeneity of the deformation operator is considered by computing the r and r_c^{max} using an intensity-based weighted distance calculation instead of a Euclidean distance calculation. Such a distance calculation can be facilitated by using the structural and functional constants associated with each voxel. In order to estimate the structural and functional constants for each voxel, we first estimate the lung deformation constants A, B, and C for the surface lung motion, which represent the structural and functional constants. The estimation of these constants has been previously discussed in [38]. Once calculated, the values of the A, B, and C are then projected from the surface to the volume using an image-based volumetric projection, which is further detailed in this section below. Now, the distance r from node j to the origin c in Eq. (1) is computed using the following formulation:

$$r_j = \frac{(A_j d(j,c) + B_j e(j,c))}{C_j} \tag{3}$$

In the above equation, the function $d(j,c)$ represents the Euclidean distance between the voxels j and c. The function $e(j,c)$ represents the difference in the regional alveolar expandability. It is to be noted that the local heterogeneity, which is represented in terms of the values A, B, C, and r_j affects the value of χ for each voxel point. The value of r_j^{max} in Eq. (1) is taken as the maximum value of r_j computed using Eq. (3). Thus, for the voxel with maximum values of values of A and B, the value of χ reaches 2π. Such heterogeneity in the assignment of χ leads to variations in the neighborhood size.

Intensity-based volumetric projection facilitates estimating the volumetric distribution of the deformation parameters A, B, and C values estimated for surface lung voxels. Let (x_j, y_j, z_j) be any voxel point inside the lung. Let (x_b, y_b, z_b) be a surface lung voxel point with known values of A, B, and C. The intensity-based weighted distance between the voxel point inside the lung and the surface boundary is computed as follows:

$$Q_b^j = e^{\sum_{p=path(j,b)}^{b} -\Delta q I(x_p, y_p, z_p)} \tag{4}$$

where Δq is the inter-voxel distance. It can be seen that the distance calculated is based on the intensity of the voxels along the path from (x_j, y_j, z_j) to (x_b, y_b, z_b). It can also be seen that as the number of voxels with non-zero intensity in the path between (x_j, y_j, z_j) and (x_b, y_b, z_b) increases, the value of Q tends to 0. Let H be the list of lung surface voxels. This distance is computed for each surface lung voxel in the list H. Finally, using these weights, the value of A for (x_j, y_j, z_j) is computed as

$$A_I = \frac{\sum_{j \in H} A_j Q_j^I}{\sum_{j \in H} Q_j^I} \tag{5}$$

Similarly, the values of B and C for the voxel (x_i, y_i, z_i) are computed using the same formulation.

$$B_I = \frac{\sum_{j \in H} B_j Q_j^I}{\sum_{j \in H} Q_j^I} \tag{6}$$

$$C_I = \frac{\sum_{j \in H} C_j Q_j^I}{\sum_{j \in H} Q_j^I} \tag{7}$$

3.3. Deformation formulation using HSH transformations

The deformation equation is now described. Let the deformation operator be defined as $\rho(\alpha, \beta, \eta, \theta_0, \varphi_0, \chi_0)$ representing the amount of the force interaction between the voxel represented by the hyper-spherical coordinate (α, β, η) and the origin $(\theta_0, \varphi_0, \chi_0)$. In the above notation, the hyper-spherical notation (α, β, η) refers to a local representation with respect to the origin. Since the heterogeneous nature of the deformation operator has been addressed during the hyper-spherical harmonic parameterization stage (Section 3.2), we now consider the operator to be homogeneous along the hyper-angle χ. Thus the deformation operator can be simplified as follows:

$$\rho(\alpha, \beta, \eta, \theta_0, \varphi_0, \chi_0) = \rho\big(\alpha, \beta, \theta_0, \varphi_0, |\eta - \chi_0|\big) \tag{8}$$

Let $D(R_{(\theta,\varphi,\chi)}(\theta_0, \varphi_0, \chi_0))$ represent the deformation magnitude of the voxel, whose location is given the hyper-spherical coordinates (θ, φ, χ). The term $R_{(\theta,\varphi,\chi)}(\theta_0, \varphi_0, \chi_0)$ represents the SO(3) group rotation of the origin $(\theta_0, \varphi_0, \chi_0)$ by the angle (θ, φ, χ). Such a group rotation term enables us to define the deformation equation in terms of the origin and then subsequently rotate the origin to the location given by (θ, φ, χ). It is to be noted from literature that the SO(4) is generally used for representing HSH rotations. Such a group rotation would include 3 rotations for each of the angles and 1 local coordinate frame rotation. In our case, the deformation operator homogeneity discussed in Eq. (8) reduces the group rotation from SO(4) to SO(3) as the local coordinate frame rotation vanishes. Such a reduction of the group rotation from SO(4) to SO(3) ultimately enables us to simplify the formulation.

Let $F(R_{(\theta,\varphi,\chi)}(\alpha,\beta,\eta))$ represent the force applied on the voxel (α,β,η), which is rotated by the angle (θ,φ,χ). The deformation equation is written as

$$D\big(R_{(\theta,\varphi,\chi)}(\theta_0,\varphi_0,\chi_0)\big) = \int_{\alpha=0}^{\pi}\int_{\beta=0}^{\pi}\int_{\eta=0}^{2\pi} F\big(R_{(\theta,\varphi,\chi)}(\alpha,\beta,\eta)\big)\rho(\alpha,\beta,\eta,\theta_0,\varphi_0,\chi_0)\,\mathrm{d}\alpha\,\mathrm{d}\beta\,\mathrm{d}\eta \tag{9}$$

We now expand each of the coefficients using HSH formulation. The applied force is expanded as

$$F\big(R_{(\theta,\varphi,\chi)}(\alpha,\beta,\eta)\big) = \sum_{\lambda_1=0}^{N}\sum_{l_1=0}^{\lambda_1}\sum_{m_1=-l_1}^{l_1}\sum_{n_1=-l_1}^{l_1} F_{\lambda_1 l_1 m_1} Y_{\lambda_1 l_1 n_1}(\alpha,\beta,\eta) S_{\lambda_1 m_1 n_1}(\theta,\varphi,\chi) \tag{10}$$

In the above equation, the term $S_{\lambda_1 l_1 m_1}(\theta,\varphi,\chi)$ represents the 3D HSH transformation of the SO(3) rotation. It is expanded as follows:

$$S_{\lambda lm}(\theta,\varphi,\chi) = s_{\lambda lm}(\theta)e^{il\varphi}e^{im\chi} \tag{11}$$

$$s_{\lambda lm}(\beta) = \frac{(-1)^{l-m}}{(l-m)!}\sqrt{\frac{(\lambda+m)!(\lambda-m)!}{(\lambda-m)!(\lambda+m)!}}\varepsilon^{(l-m)/2}(1-\varepsilon)^{(l+m)/2}J(L-M,2M+1,M-K+1,\varepsilon) \tag{12}$$

$$\varepsilon = \sin^2(\beta/2) \tag{13}$$

where J represents the Jacobi's polynomial, which can be expanded as follows:

$$J(p,a,b,x) = \sum_{r=0}^{P}\frac{(b-1)!(a-b+p)!p!(-x)^{P-r}(1-x)^r}{(p-r)!r!(b-1+p-r)!(a-b+r)!} \tag{14}$$

Additionally, the function $Y_{\lambda_1 l_1 m_1}$ in Eq. (10) represents the HSH transformation of the input data. It is expanded as follows:

$$Y_{\lambda_1 l_1 m_1}(\theta,\varphi,\chi) = N_{\lambda_1 l_1}\sin^l(\chi)G_{\lambda-l}^{1+l}(\cos\chi)P_{\lambda_1 l_1}(\theta,\varphi) \tag{15}$$

where the function G represents the Gegenbauer polynomial and the function P represents the Legendre polynomials. The normalizing term N is expanded as follows:

$$N_{\lambda_1 l_1} = \left(\frac{2}{\pi}\frac{(2l_1)!!(\lambda+1)(\lambda-l)!!(2l+1)!}{(2l+1)!!(\lambda+l+1)!}\right)^{1/2} \tag{16}$$

Similarly the deformation operator is expanded as follows:

$$\rho\big((\alpha,\beta,\eta),(\theta_0,\varphi_0,\chi_0)\big) = \sum_{\lambda_2=0}^{N}\sum_{l2=0}^{\lambda_2}\sum_{\lambda_2^1=0}^{N}\sum_{l_2^1=0}^{\lambda_2^1}\sum_{m_2^1=-l_2^1}^{l_2^1} \rho_{\lambda_2 l_2 \lambda_2^1 l_2 l^1 m_2^1} Y^*_{\lambda_2 l_2 m_2^1}(\theta_0,\varphi_0,\chi_0) Y_{\lambda_2^1 l_2^1 m_2^1}(\alpha,\beta,\eta) \tag{17}$$

Incorporating the expansions given in (17) and (10) into (9) we obtain the expansion of the deformation in the hyperspherical coordinates as follows:

$$\begin{aligned} &D\big(R_{(\theta,\varphi,\chi)}(\theta_0,\varphi_0,\chi_0)\big) \\ &= \sum_{\lambda_1=0}^{N}\sum_{l_1=0}^{\lambda_1}\sum_{m_1=-l}^{l_1}\sum_{n_1=-l_1}^{l_1}\sum_{\lambda_2=0}^{N}\sum_{l_2=0}^{\lambda_2}\sum_{\lambda_2^1=0}^{N}\sum_{l_2^1=0}^{\lambda_2^1}\sum_{m_2^1=-l_2^1}^{l_2^1} f_{\lambda_1 l_1 m_1}\rho_{\lambda_2 l_2 \lambda_2^1 l_2^1 m_2^1} S_{\lambda_1 m_1 n_1}(\theta,\varphi,\chi) Y_{\lambda_2^1 l_2^1 m_2^1}(\theta_0,\varphi_0,\chi_0) X_{\lambda_1 l_1 n_1 \lambda_2^1 l_2^1 m_2^1} \end{aligned} \tag{18}$$

In the above equation, the term $X_{\lambda_1 l_1 n_1 \lambda_2^1 l_2^1 m_2^1}$ represents the angular integration component of Eq. (9) and is expressed as follows:

$$X_{\lambda_1 l_1 n_1 \lambda_2^1 l_2^1 m_2^1} = \int_{\alpha=0}^{\pi}\int_{\beta=0}^{\pi}\int_{\eta=0}^{2\pi} Y_{\lambda_1 l_1 n_1}(\alpha,\beta,\eta) Y^*_{\lambda_2^1 l_2^1 m_2^1}(\alpha,\beta,\eta)\,\mathrm{d}\alpha\,\mathrm{d}\beta\,\mathrm{d}\eta \tag{19}$$

Eq. (19) can be represented using Dirac delta functions as it is an integral of conjugate orthogonal functions.

$$X_{\lambda_1 l_1 n_1 \lambda_2^1 l_2^1 m_2^1} = \delta_{\lambda_1 \lambda_2^1}\delta_{l_1 l_2^1}\delta_{n_1 m_2^1} \tag{20}$$

Using Eq. (20), we set $\lambda_1 = \lambda_2^1$, $l_1 = l_2^1$, and $n_1 = m_2^1$ as terms that do not satisfy this condition compute to 0. Eq. (18) can thus be further simplified as follows:

$$D\big(R_{(\theta,\varphi,\chi)}(\theta_0,\varphi_0,\chi_0)\big) = \sum_{\lambda_1=0}^{N}\sum_{l_1=0}^{\lambda_1}\sum_{m_1=-l_1}^{l_1}\sum_{\lambda_2=0}^{N}\sum_{l_2=0}^{\lambda_2}\sum_{n_1=-l_1}^{l_1} f_{\lambda_1 l_1 m_1}\rho_{\lambda_1 l_1 \lambda_2 l_2 n_1} S_{\lambda_1 m_1 n_1}(\theta,\varphi,\chi) Y_{\lambda_2^1 l_2^1 n_1}(\theta_0,\varphi_0,\chi_0) \tag{21}$$

We now expand the deformation term on the left-hand side to represent the expansion in terms of the HSH coordinates. We write the HSH expansion of the left-hand side as follows:

$$D\big(R_{(\theta,\varphi,\chi)}(\theta_0,\varphi_0,\chi_0)\big) = \sum_{\lambda_1^2=0}^{N}\sum_{l_1^2=0}^{\lambda_1^2}\sum_{m_1^2=-l_1}^{l_1^2}\sum_{\lambda_2^2=0}^{N}\sum_{l_2^2=0}^{\lambda_2^2}\sum_{n_1^2=-l_1^2}^{l_1^2} d_{\lambda_1^2 l_1^2 m_1^2 \lambda_2^2 l_2^2 n_2^2} S_{\lambda_1^2 m_1^2 n_1^2}(\theta,\varphi,\chi) Y_{\lambda_2^2 l_2^2 n_1^2}(\theta_0,\varphi_0,\chi_0) \tag{22}$$

Finally, equating the frequency coefficients of Eq. (22) with (21), we obtain the following key relation to our model:

$$d_{\lambda_1 l_1 m_1 \lambda_2 l_2 m_2} = \left(\frac{8\pi^2}{2\lambda_1+1}\right) f_{\lambda_1 l_1 m_1}\rho_{\lambda_1 l_1 \lambda_2 l_2 m_2} \tag{23}$$

In the above equation, the term $\frac{8\pi^2}{2\lambda_1+1}$ refers to the normalization factor of the SO(3) rotation group. Thus from Eq. (23), it can be seen that for known values of displacement and applied force, which are represented by their HSH coefficients, the deformation operator can be estimated in terms of their spherical harmonic coefficients. It is to be noted that the estimated deformation operator is associated with the voxel point, which was considered as the center in Eq. (1). The estimated values of the deformation operator are also specific to the human subject and so can vary from one subject to another. A means of estimating the applied force is discussed along with the implementation details in Section 4.

3.4. Estimation of YM

We now solve for the YM using the estimated deformation operator. In order to estimate the YM associated with each voxel point, the general problem of indentation of the half space by a frictionless rigid force is considered [17]. Mathematically, a mixed boundary-value problem for the potential function is considered. Considering a normal traction and a set of normal forces, the normal surface displacement is given as

$$u_x(n) = \frac{(1-\nu)}{2\pi\mu}\int_{Area}\frac{p_x(\varepsilon)\,\mathrm{d}\varepsilon}{r(\varepsilon,n)} \tag{24}$$

where the ν represents the Poisson ratio, μ represents the Lame's constant, and $r(\varepsilon,n)$ represents the Euclidean distance between the voxel points ε and n. Extending to voxel specific elasticity parameters, Eq. (24) can be written in terms of the elastic properties associated with each voxel as

$$u_x(n) = \frac{(1-\nu_n)}{2\pi\mu_n}\int_{Area}\frac{p_x(\varepsilon)\,\mathrm{d}\varepsilon}{r(\varepsilon,n)} \tag{25}$$

Considering the singularity conditions $\varepsilon = n$, setting ν_n to 0.43 as established in the literature, the elasticity parameters can be equated to the deformation operator as

$$\rho(n,n) = \frac{0.1066}{\mu_n} \tag{26}$$

The YM (E_n) of voxel n can be directly computed using the Lame's constant and the Poisson ratio using the following known relation:

$$E_n = 2\mu_n(1+\nu_n) \tag{27}$$

4. Implementation

4.1. 4D-CT data acquisition

4D-CT datasets for a human subject at 10% tidal volume intervals were taken using Siemens Biograph Strain-gauge 64 slices CT. The 3D volumetric lung and the airways were segmented using Pinnacle MBS, and OSIRIX software.

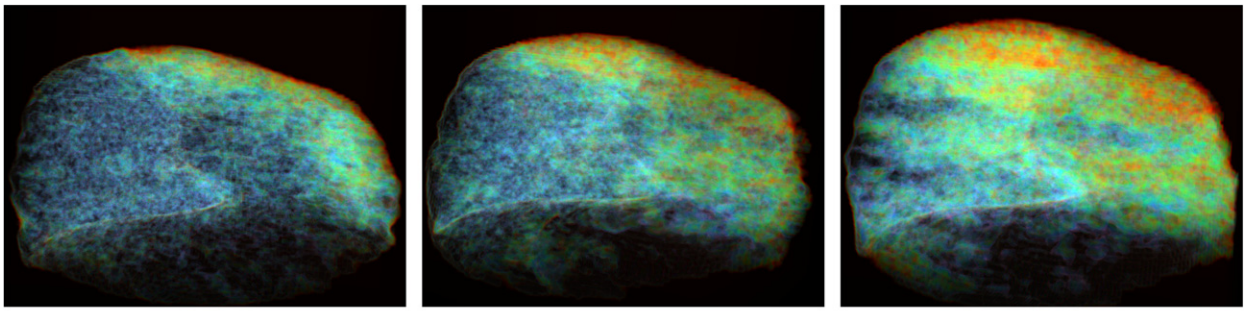

Fig. 2. A volume rendered 3D distribution of the lung displacement along the cranio-caudal direction from (a) 0–30%, (b) 0–60% and (c) 0–100% tidal lung volume.

4.2. 4D-CT registration using optical flow

First, the 4D-CT data registration algorithm was used to estimate the motion of each 3D voxel in one 3D volume data by searching for and locating a corresponding voxel in another 3D volume with similar intensity and closer to the same location. Mathematically, the optical flow motion estimation is based on local Taylor series approximation and is further described in the optical flow literature [4]. One of the limitations of the optical flow method as it applies to estimating the 3D organ motion is the low sensitivity to variations in regional motion. In order to improve the accuracy of optical flow algorithm implementation we use the multi-level multi-resolution optical flow method [39], which computes optical flow between two 3D volumes at lower resolution, propagates the result to the higher resolution volume and subsequently to the original resolution volume data [3]. In this approach, the organ anatomy is separated into four parts: (1) lung outline, (2) large capillaries, (3) small capillaries, and (4) parenchymal region. At each level of anatomy optical flow, a multi-level multi-resolution optical flow registration is used for computing the 4D organ motion of that anatomy and integrated into the next level. Results are shown in Fig. 2, where the 3D volumetric lung motion is encoded in the continuous color range of black (0 mm), red (1 mm), green (2 mm) and blue (4 mm). It can be seen from the images that the lung volume deforms during breathing.

4.3. Estimation of the applied force

The applied force is determined using spirometry measurements that dictate the pressure and volume of the air that entered the lung during a given change in lung volume and the pressure gradient imposed by the gravity from the apex to the base. Thus the known amount of air pressure is distributed inside the lungs according to the pressure gradient. This distribution of air, which subsequently leads to the change in lung shape, is taken as the applied force.

4.4. Estimation of the volumetric lung deformation operator

As a first step, the surface lung deformation operator is extracted from the 4D-CT using the method discussed in [3]. The structural and functional constants of the surface lung are then projected onto the lung volume using the method presented in Section 3.3. The HSH parameterization is then performed for each node (Sections 3.1 and 3.2). Once parameterized, the deformation operator for each node is then estimated. In order to address the excessive run-time problem, a Streaming SIMD Extensions 4 (SSE4) is employed and the transformations are programmed using the "Accelerate" framework, which encapsulate the SSE4 instructions as a set of high-level functions. This framework enables us to use the Intel processors as parallel vector processors thereby facilitating enhancements in computational speed.

Fig. 3 shows the surface lung displacement (Fig. 3(a)) as vectors from the surface lungs in supine position. It can be seen that the magnitude of the lung displacement in supine position varies from one region to another. The subsequent surface lung deformation constants estimated from the displacement are shown (Figs. 3(b) and 3(c)). The values in this case are normalized and color-coded between red (0) and white (1). These constants are then projected into the lung volume using the barycentric intensity-based interpolation method. Figs. 4(a) and 4(b) show the projected constants as normalized and color-coded values. The structural and functional constants are normalized such that 0, 0.3, 0.6, 0.9, 1.0 are represented by the colors black, blue, green, red, and white, respectively. These constants are then used to compute the neighborhood for the HSH parameterization.

The estimated value of YM for each voxel is as shown in Figs. 5(a) and 5(b) as normalized and color-coded values. The value of YM for each voxel estimated using the proposed method has a mean value of 0.7 kPa with a standard deviation of 0.4 kPa. Such a range of YM values is in accordance with the value range discussed in [10]. The color-coding is done in such a way that the values 0, 0.2, 0.4, 0.6, 0.8 and 1. 0 are represented by the colors black, red, yellow, green, blue and white, respectively. The key observations that can be made are as follows. First the region inside the lung that is closer to the

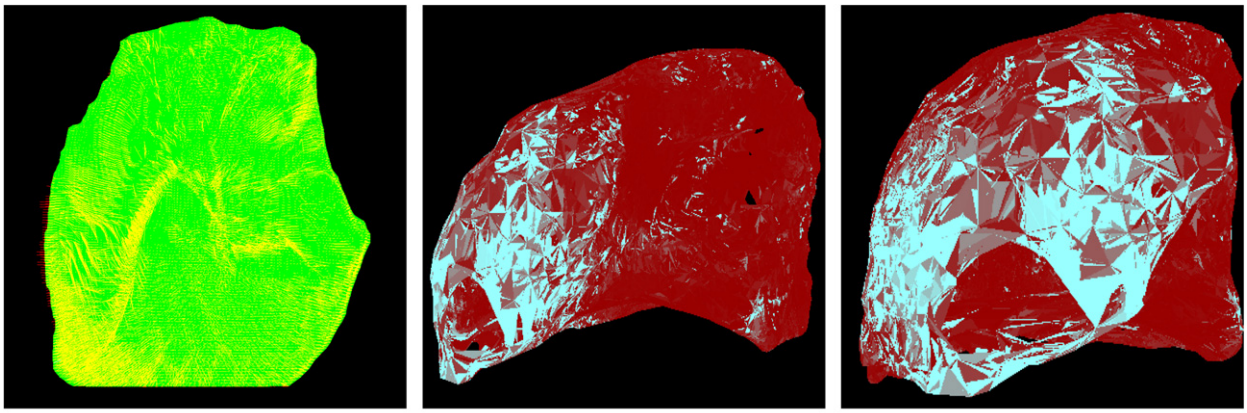

Fig. 3. A surface displacements are as vectors (in yellow) propagating from the surface of the lungs as shown for supine orientation in (a). The estimated surface lung deformation constants and A and B are shown for upright orientation in (b) and (c), respectively. The values are normalized and color-coded between red (0) and white (1).

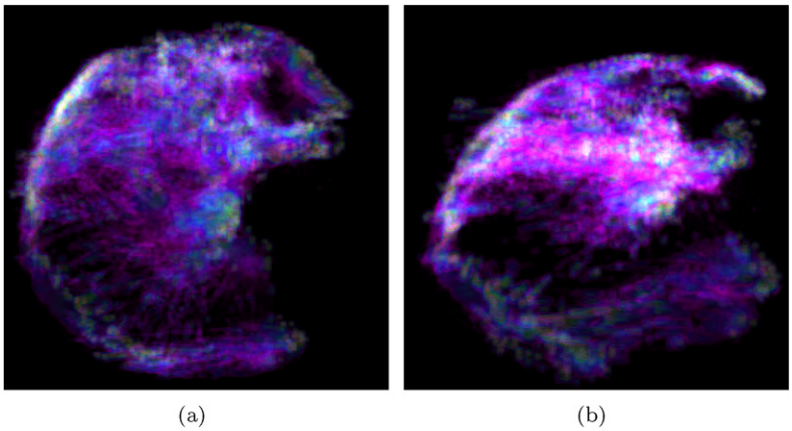

Fig. 4. Barycentric intensity-based interpolation of the structural constant A is shown in front (a) and side (b) view. The values are computed from the structural constants estimated from the inverse surface lung deformation analysis.

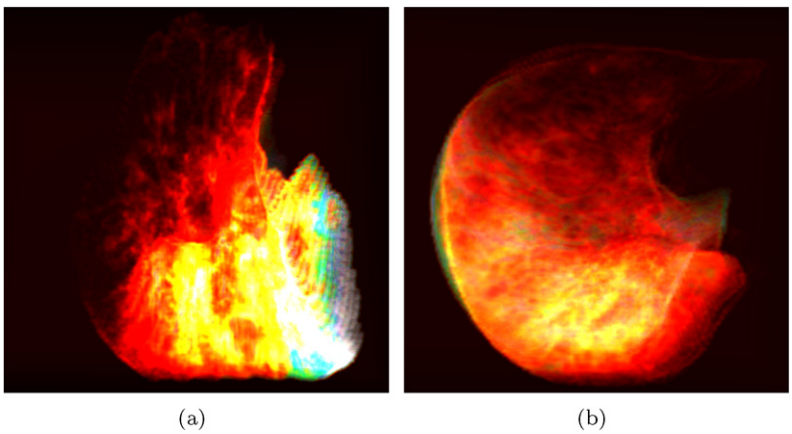

Fig. 5. The volumetric distribution of the Young's Modulus is shown for the left lung at two different view angles: supine sidewise (a) and supine cranio-caudal (b). The Young's Modulus values are color-coded from red (lowest) to yellow, green, blue and white (highest).

diaphragm has a higher YM value as compared to the region that is distal from the diaphragm. However, the capillaries and the airways can be seen with a higher YM value in the region closer to the apex of the lung. Thus the estimated YM value shows a clear distinction between the tissues whose YM is being estimated. Second, the region inside the lung closer to the

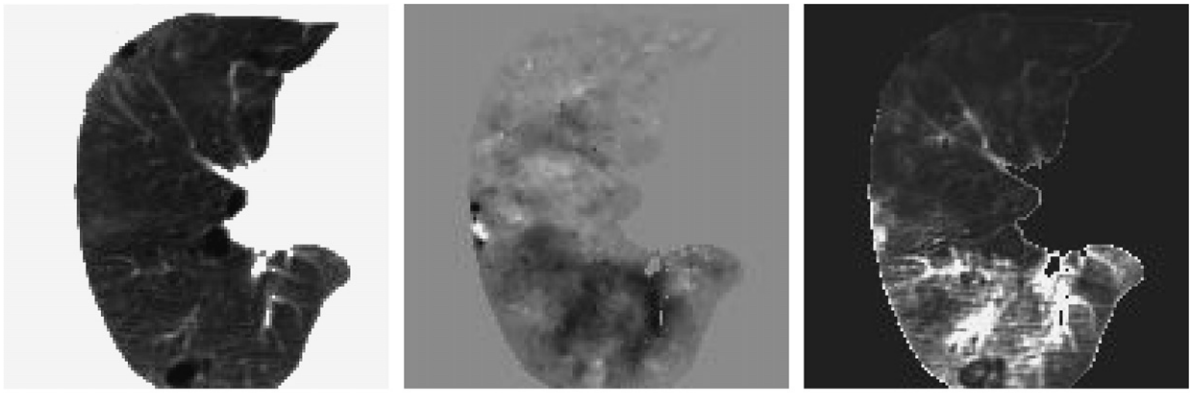

Fig. 6. The 2D slice of the original lung anatomy is shown in (a). The voxel displacement and the YM value associated with each of voxel of (a) is shown in (b) and (c), respectively.

posterior base has a higher YM as compared to the region near the anterior base. This can be correlated with the fact that the displacement near the posterior base is higher than the anterior base as shown in Fig. 3(a). Finally, such correlations are specific to a patient. It can be seen that YM distribution can be effectively used to better understand the lung functionality of the region being treated using radiotherapy.

Fig. 6(a) shows a 2D cranio-caudal slice representation of the voxels along the middle of the left lung. The block spherical regions represent the air pockets that have accumulated inside the lung. The grey-scale mappings of the 3D displacement of these voxels are shown in Fig. 6(b) revealing the motion of the air pockets. The estimated YM value of each voxel is grey-scale mapped and shown in Fig. 6(c). Two key observations that can be made are as follows. First, it can be seen that the capillaries inside the lung have a higher YM than the surrounding tissue region, which agrees with the fact that the capillaries are thicker than the parenchymal tissue. Second, it can be seen that the air pocket-like voxels in the 3D slice are shown to have a very low YM value. This observation agrees with the fact the air has a very low YM value. Additionally, from Fig. 6(c), the local variations in the estimated YM value can be correlated with the local anatomy although these anatomical regions do not clearly show such distinctions in the 3D volumetric displacement used as the input for the inverse analysis.

4.5. Complexity analysis

In this section, we discuss the computational complexity of the intensity-based volumetric projection method discussed in Section 3.3 and the estimation of the deformation operator discussed in Section 3.4. One of the key limitations of the intensity-based volumetric projection is that the computational complexity of this projection is approximately $O(I^I)$, where I is the total number of volumetric lung voxels. In the case of a 3D lung CT data at resolution (1 mm $\times$ 1 mm $\times$ 3 mm), such an interpolation takes 150 hours to compute on an 8-core Mac Pro workstation. However, recent advances in the parallel computational capability facilitated by Graphical Processing Units have led to the reduction of the computation time for such complex problems. We employed an NVIDIA 8800GT graphics card to perform the computation. The 3D-CT data of the volumetric lung was loaded into the graphics card as a 3D texture. For each voxel point, the calculation of the weights was done in parallel. Results showed that Eq. (4) was calculated for all the lung voxels in approximately 60 seconds.

Two key limitations of the method for estimating the deformation operator are the run-time complexity and the memory complexity. While the run time complexity analysis shows that it takes approximately $O(V2)$ calculations, where V is the total number of lung voxels, it tooks approximately one second to estimate the deformation operator for each voxel. Thus for one lung, thus total estimation time is approximately 80 hours, which is quite high. However, the calculation time can be considerably reduced by setting a smaller neighborhood size in Section 3.1 and using state-of-art graphics processors to perform the calculations. The memory complexity for the method is also $O(V2)$, which make the method expensive given a high value of V. Reducing the neighborhood size leads to the reduction of the complexity $O(V * W)$, where W is the neighborhood size.

5. Validation of proposed method

We now discuss the steps taken for the validation of the proposed method in estimating the 3D deformation operator. Four different computer-based experimental setups are considered. In each of the experimental setups, we consider a 3D cube of voxels as the input data. We intend to first simulate a deformation of a 3D cube composed of voxels, for a given friction-less applied force and a pre-assigned YM associated with each voxel, and then re-estimate the YM associated with each cube using the deformation and the applied force. A known amount of force (1 Newton) is applied on the center of the tissue as a frictionless rigid indentation as shown in Fig. 7(a). The displacement of each voxel is computed as shown in Eq. (24) using constant value of YM (50 Pa, 100 Pa, 200 Pa, 400 Pa) for each voxel during each of the four experiments.

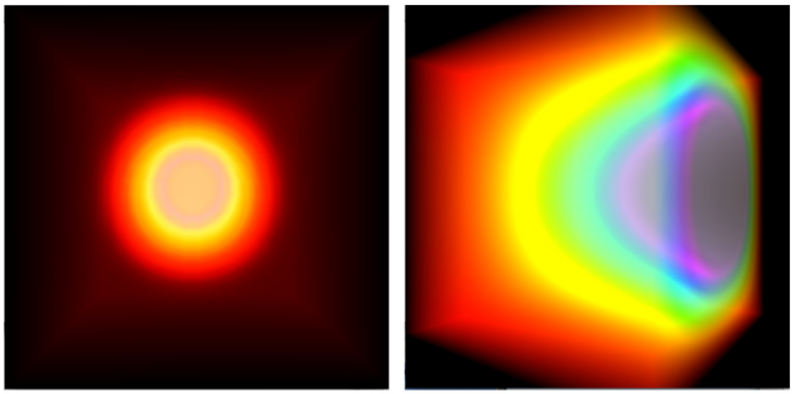

Fig. 7. (a) The 3D distribution of the applied force on a 3D cube of tissue and the corresponding displacement of the 3D tissue. (b) The colors represent a continuous range of 0.25 (red), 0.5 (yellow), 0.7 (green) and 0.9 (blue) and 1.0 (violet).

Table 3
Validation results of the actual and the predicted YM values.

Actual YM (Pa)	Predicted YM (Pa)
50	50.03 ± 0.25
100	98.94 ± 0.03
200	198.87 ± 0.14
400	402.83 ± 0.02

Such a usage of constant YM allows us to use a constant neighborhood size during the inverse analysis. For the known displacement and the applied force, we estimate the YM for each voxel using the formulation discussed in Eq. (24). Fig. 7(b) shows the displacement of each voxels for a YM value of 400 Pa. The displacements are normalized and color-coded such that the normalized displacement units 0.25, 0.5, 0.7, 0.9 and 1.0 are represented by the red, yellow, green, blue and violet, respectively. Results are tabulated in Table 3. These validations show that the YM values can be estimated within ± 2 Pa range, which is approximately 1% variation from the assigned YM value.

6. Conclusion and future work

A new method to estimate the elastic properties of 3D volumetric lungs in order to re-construct the 3D lung deformations under different breathing conditions is discussed in this paper. The method takes as input the subject-specific airflow and lung deformations estimated from 4D-CT imaging data coupled with spirometry. An HSH expansion of the coefficients is done in order to estimate the deformation operator for each voxel point of the lung for known values of the applied force and the displacement. From a clinical perspective, such an estimation of the deformation operator also allows us to re-construct and simulate 3D lung deformation for different breathing conditions. Additionally, the regional distribution of the YM can be correlated with the patho-physical condition of the subject. Such a correlation can ultimately be used for optimizing the radiotherapy treatment plan to spare vulnerable tissues in the vicinity of the lung tumor.

From a mathematical perspective, the proposed formulation of the volumetric lung deformation employs the Gegenbauer polynomials to represent the applied force, which in the case of lungs is known to have a smooth distribution. The lung voxel displacement, which has a coarse distribution as estimated using 3D optical flow technique, is represented using Wigner-d polynomials. Such a representation facilitates a loss-less representation in the frequency domain using a finite number of frequency coefficients. The estimated deformation operator, which represents the elastic interaction between voxels in the neighborhood, facilitates re-constructing the 3D lung deformations for different breathing conditions represented as variations in the applied force.

Results show the volumetric distribution of the YM for two lungs, which clearly shows the local variations in the elastic property. Additionally, the estimated YM value associated with individual voxel can be correlated with the local anatomy (as shown in Fig. 6), which reveals the localized variation between the tissue and the capillaries. Validation results are shown using a computer-based 3D virtual cube representing tissue with a pre-assigned YM value for each voxel. A friction-less rigid force indentation is considered (as shown in Fig. 7). Using the deformed tissue, the YM value associated with each voxel is re-constructed and tabulated. Results show that the values are estimated with ± 2 Pa variations. Future work will include further validations using heterogeneous tissue elastic properties and different types of 3D geometry.

From an implementation perspective, the proposed formulation is shown to be expensive in terms of both computational as well as memory requirements. Future work will involve investigating the computational accuracy when the memory requirements and the computational complexity are reduced. For instance, the usage of a smaller neighborhood for each

voxel as compared to considering the entire lung in the neighborhood will facilitate faster and cheaper estimation of the deformation operator and subsequently the YM associated with each voxel. Also, modern graphics processing units will be investigated for reducing the computational time taken for performing the calculations.

Acknowledgement

This research was carried out under a grant from the Florida Department of Health James and Esther King Biomedical Research Program.

References

[1] D.N. Metaxas, Physics-Based Deformable Models, Kluwer Publishers, Philadelphia, PA, 1997.
[2] M.J. Murphy, Tracking moving organs in real time, Seminars on Radiation Oncology 14 (1) (2004) 91–100.
[3] H. Shirato, Y. Seppenwoolde, K. Kitamura, R. Onimura, S. Shimizu, Intrafractional tumor motion: lung and liver, Seminars on Radiation Oncology 14 (1) (2004) 10–18.
[4] R. De Wilde, J. Clement, J.M. Hellemans, M. Decramer, M. Demedts, R. Boving, K.P. Van de Woestijne, Model of elasticity of the human lung, Journal of Applied Physiology 51 (1981) 254–261.
[5] J.H. Leite-Junior, P.R.M. Rocco, D.S. Faffe, P.V. Romero, W.A. Zin, On the preparation of lung strip for tissue mechanics measurement, Respiratory Physiology & Neurobiology 134 (3) (2003) 255–262.
[6] J.P. Butler, M. Nakamura, H. Sasaki, T. Sasaki, T. Takishima, Poisson's ratio of lung parenchyma and parenchymal interaction with bronchi, Japan Journal of Physiology 36 (1) (1986) 91–106.
[7] Y.C. Fung, Biomechanics, Mechanical Properties of Living Tissues, 2nd ed., Springer-Verlag, New York, 1993.
[8] A. Adler, E.A. Cowley, J.H.T. Bates, D.H. Eidelman, Airway-parenchymal interdependence after airway contraction in rat lung explants, Journal of Applied Physiology 85 (1998) 231–237.
[9] T. Ebihara, N. Venkatesan, R. Tanaka, M.S. Ludwig, Changes in extracellular matrix and tissue viscoelasticity in bleomycin-induced lung fibrosis, Americal Journal of Respiratory Critical Care Medicine 162 (4) (2000) 1569–1576.
[10] B.C. Goss, K.P. McGee, S.A. Kruse, A. Manduca, R.L. Ehman, Magnetic resonance elastography of the lung: Initial feasibility, Proceedings of International Society of Magnetic Resonance in Medicine 11 (2003) 429.
[11] Ilya Levental, Penelope C. Georges, Paul A. Janmey, Soft biological materials and their impact on cell function, Soft Matter 3 (2007) 299–306.
[12] K.K. Brock, M.B. Sharpe, L.A. Dawson, S.M. Kim, D.A. Jaffray, Accuracy of finite element model-based multi-organ deformable image registration, Medical Physics 32 (6) (June 2005) 1647–1659.
[13] R. Werner, J. Ehrhardt, R. Schmidt, H. Handels, Modeling respiratory lung motion a biophysical approach using finite element methods, in: Proc. SPIE, vol. 6916, San Diego, USA, February 2008, 69160N.
[14] F. Liu, B. Shea, J. Mih, A. Tager, D. Tschumperlin, Lung parenchymal tissue stiffness in fibrosis and cellular responses to substrate stiffness, Biophysical Journal 96 (3) (2009) 395a.
[15] F.S. Cavalcante, S. Ito, K. Brewer, H. Sakai, A.M. Alencar, M.P. Almeida, J.S. Andrade, A. Mujumdar, E.P. Ingenito, B. Suki, Mechanical interactions between collagen and proteoglycans: implications for the stability of lung tissue, Journal of Applied Physiology 98 (2005) 672–679.
[16] L.S. Wilson, D.E. Robinson, M.J. Dadd, Elastography – the movement begins, Physics for Medicine and Biology 45 (6) (2000) 1409–1421.
[17] J.R. Barber, Elasticity, in: G.M.L. Gladwell (Ed.), Solid Mechanics and Its Applications, Kluwer Academic Publisher, Waterloo, Canada, 1992.
[18] J.C. Gee, T. Sundaram, I. Hasegawa, H. Uenatsu, H. Hatabu, Characterization of regional pulmonary mechanics from serial MRI data, in: Medical Image Computing and Computer Aided Intervention, in: Lecture Notes on Computer Science, 2002, pp. 762–769.
[19] J.B. Weaver, E.E.W. Van Houten, M.I. Miga, F.E. Kennedy, K.D. Paulsen, Magnetic resonance elastography using gradient echo measurement of steady-state motion, Medical Physics 28 (8) (2001) 2001.
[20] A. Pentland, B. Horowitz, Recovery of nonrigid motion and structure, IEEE Transactions on Nuclear Science 13 (7) (1991) 730–742.
[21] A.L. Bukhgeim, Introduction to the Theory of Inverse Problems, Inverse and Ill-Posed Problems Series, VSP, Utrecht, 2000.
[22] D.N. Metaxas, Elastically adaptive deformable models, IEEE Transactions on Pattern Recognition 24 (10) (2002) 1310–1322.
[23] I. Stakgold, Green's Functions and Boundary Value Problems, Mathematical Physics, Wiley Interscience, 1979.
[24] R.E. White, An Introduction to Finite Element Methods, John Wiley and Sons, Raleigh, NC, 1991.
[25] A. Santhanam, T. Willoughby, S.L. Meeks, J.P. Rolland, P. Kupelian, Real-time simulation of 4D lung tumor radiotherapy using a breathing model, in: Medical Image Computing and Computer Aided Intervention (2), 2008, pp. 710–717.
[26] M.M. Doyley, P.M. Meaney, J.C. Bamber, Evaluation of an iterative reconstruction method for quantitative elastography, Physics in Medicine and Biology 45 (2000) 1521–1540.
[27] R. Ramamoorthi, P. Hanrahan, On the relationship between radiance and irradiance: Determing the illumination from images of a convex Lambertian object, Journal of Optical Society of America (2001) 2448–2459.
[28] J.C. Adams, P.N. Swartztrauber, Spherepack 2.0: A model development facility, NCAR Technical note NCAR/TN-436-STR, 1997.
[29] A. Santhanam, F.G. Hamza-lup, J.P. Rolland, Simulating 3D lung dynamics in a programmable graphics processing unit, IEEE Transactions on Information Technology and Biomedicine 11 (5) (2006) 497–506.
[30] J. Avery, Hyperspherical Harmonics and Generalized Sturmians, Progress in Theoretical Chemistry and Physics, Kluwer Academic Publishers, Boston, MA, 2000.
[31] A. Kupperman, J.A. Kaye, J.P. Dwyer, Hyper spherical coordinates in the quantum mechanical collinear reactive scattering, Chemical Physics Letters 74 (1980) 257.
[32] V. Aquilanti, S. Cavalli, A. Lagana, Hyperspherical description of interference effects and resonances in collinear chemical reactions, Chemical Physics Letters 93 (1982) 174.
[33] R.K. Peterkop, Theory of Ionization of Atoms by Electron Impact, Colorado Associated University Press, Boulder, CO, 1977, Translated by D.G. Hummer, E. Aronson.
[34] T. Shibuya, C.E. Wulfman, Molecular orbital in momentum space, Proceedings of Royal Society A 286 (1965) 376.
[35] W. Rudin, Fourier Analysis on Groups, Interscience, New York, 1962.
[36] A. Santhanam, A. Shah, I. Kaya, J.P. Rolland, P. Kupelian, A display framework for visualizing real-time lung tumor radiotherapy, Journal of Display Technology 4 (4) (2008) 473–482.
[37] A.P. Santhanam, C. Imielinska, P. Davenport, P. Kupelian, J.P. Rolland, Modeling and simulation of real-time 3D lung dynamics, IEEE Transactions on Information Technology and Biomedicine 12 (2) (2008) 257–270.
[38] P.J. Kostelec, D.N. Rockmore, FFTs on the rotation group, Journal of Fourier Analysis and Applications 14 (2) (2008) 145–179.
[39] Y. Min, H. Neelakkantan, B.H. Ruddy, S.L. Meeks, P. Kupelian, A.P. Santhanam, A GPU based framework for real-time lung radiotherapy monitoring applications, in: Computer Assisted Radiology and Surgery International Congress and Exhibition, 2010.